The basic performance of a precipitation retrieval algorithm for the Global Precipitation Measurement mission's single/dual-frequency radar measurements

Shinta Seto, *Member*, IEEE, Toshio Iguchi, *Member, IEEE,* Taikan Oki

Manuscript submitted April 16, 2012; revised September 27, 2012. This work was supported by the Japan Aerospace Exploration Agency under the 6th Precipitation Measuring Mission Research Announcement.

S. Seto and T. Oki are with the Institute of Industrial Science, The University of Tokyo, Tokyo 153-8505, Japan (e-mail: seto@rainbow.iis.u-tokyo.ac.jp).

T. Iguchi is with the National Institute of Information and Communications Technology, Koganei, Tokyo 184-8795, Japan.

***Abstract*— A precipitation retrieval algorithm is proposed for the Dual-frequency Precipitation Radar (DPR) on the core satellite of the Global Precipitation Measurement (GPM) mission. The proposed algorithm is called the HB-DFR algorithm, in reference to the combination of Histchfeld-Bordan's attenuation correction method (HB method) and the dual-frequency ratio (DFR) method. The HB-DFR algorithm is tested with a synthetic DPR dataset produced from the standard product of the Precipitation Radar on the Tropical Rainfall Measuring Mission. Precipitation rates estimated by the HB-DFR algorithm at the lowest (near-surface) range bin are evaluated by comparing them with the corresponding values calculated from the drop size distribution of the synthetic dataset. For "light precipitation" (below 1 mm h^{-1}), precipitation rates are slightly underestimated because of the multiple-solution problem in the DFR method. For "heavy precipitation" (above 10 mm h^{-1}), the precipitation rates are severely underestimated, and the biases become large when thick liquid phase precipitation occurs. For "medium precipitation" (between 1 and 10 mm h^{-1}), the estimates are satisfactory. As almost 50% of precipitation falls as medium precipitation in the synthetic dataset, this result validates the usefulness of DPR measurements and the HB-DFR algorithm. Because the HB-DFR algorithm is a forward retrieval algorithm, it has multiple solutions and produces larger errors when applied to lower (farther) range bins. Unlike other dual-frequency algorithms, the HB-DFR algorithm can be easily switched to a single-frequency algorithm at a range bin where a measurement at one of the two frequencies is not available.**

***Index Terms*—Attenuation, radar, rain.**

I. INTRODUCTION

The Dual-frequency Precipitation Radar (DPR) on the core satellite of the Global Precipitation Measurement (GPM) mission is composed of two radars: KuPR (13.6 GHz) and KaPR (35.5 GHz). KuPR is similar to the Tropical Rainfall Measuring Mission (TRMM) Precipitation Radar (PR; 13.8 GHz). The DPR has three objectives: (I) continuation of PR-like measurements by KuPR, (II) detection of solid and/or light precipitation by KaPR, and (III) accurate estimation of the drop size distribution (DSD) and precipitation rates by simultaneous measurements with KuPR and KaPR.

Fig. 1 schematically shows observations by DPR. KuPR operation is similar to that of PR; there are 49 pixels in a normal scan with the swath width of 245 km. At each pixel, precipitation and surface echoes are measured with a vertical resolution of 250 m (oversampled data are available at an interval of 125 m). When KuPR observes a pixel in the inner part of a normal scan, KaPR observes the same pixel with the same vertical resolution. When KuPR observes pixels in the outer part of a normal scan, KaPR produces an interleaved scan and observes pixels in the inner swath with a vertical resolution of 500 m (oversampled data are available at the interval of 250 m). The coarser vertical resolution in interleaved scans makes it possible to detect lighter precipitation; the minimum detection level is 18 dBZ in a normal scan, but is reduced to 12 dBZ in an interleaved scan. There are three types of pixels: those (A) measured by KuPR only, (B) measured by KaPR only, and (C) measured both by KuPR and KaPR. Pixel types (A) to (C) correspond to objectives (I) to (III).

For each pixel type, a precipitation retrieval algorithm must be developed. For pixel type (A), a single-frequency (KuPR) algorithm can be developed based on the PR standard algorithm [1], [2]. The PR standard algorithm adopts a hybrid method with Hitschfeld-Bordan's attenuation correction method (HB method) [3] and the surface reference technique (SRT). The basic structure of the PR standard algorithm is also applicable to a single-frequency (KaPR) algorithm for pixel type (B), although the differences in frequency and vertical resolution need to be considered.

For pixel type (C), there are a few dual-frequency algorithms proposed in previous studies. Some of these can retrieve two DSD parameters per range bin. Meneghini *et al.* [4] applied a backward retrieval algorithm (BRA), where the DSD parameters are retrieved from the bottom to the top with path integrated attenuation (PIA) estimated by the SRT. Generally, the BRA is robust compared with forward retrieval algorithms (FRAs). This is because the lower boundary condition is given in the BRA, while errors in attenuation can accumulate wrongly and may diverge in FRAs. However, BRA estimations depend largely on the SRT, which is sometimes inaccurate over land. Mardiana *et al.* [5] developed an iterative backward retrieval algorithm (IBRA) that did not use the SRT. In the IBRA, PIA is arbitrarily assumed and the BRA is applied until the boundary condition at the top of the precipitation is satisfied. The IBRA is equivalent to an FRA and it has multiple solutions [6]. As the IBRA tends to select a solution with smaller precipitation rates among multiple solutions, it yields underestimations for heavy precipitation [6]-[8]. To get unique and better solution in a dual-frequency algorithm, differential attenuation constraint [8] and DSD constraint [9] are proposed.

The above dual-frequency algorithms are developed independently of single-frequency algorithms such as the PR standard algorithm. However, consistency between single- and dual-frequency algorithms is desired for the DPR to produce a seamless three-dimensional field of the precipitation rate estimates. In this paper, a precipitation rate retrieval algorithm, which is applicable both for single-frequency and dual-frequency measurements is proposed. The proposed algorithm is termed the HB-DFR algorithm, because the HB method is applied in combination with the DFR method. We propose the HB-DFR algorithm as part of a baseline algorithm for the DPR standard algorithm and demonstrate the potential and limitations of this algorithm. Because the SRT is not used in the HB-DFR algorithm, robustness cannot be expected. In future work we propose to involve the SRT to make the HB-DFR algorithm more accurate and robust for the DPR standard algorithm.

The remainder of this paper is organized as follows. In Section II, the synthetic DPR dataset that we use to test and evaluate the HB-DFR algorithm is described. In Section III, the operation of the HB-DFR algorithm

as a fully dual-frequency algorithm is explained. Then, the HB-DFR algorithm is applied to a synthetic dataset and general evaluations are presented in Section IV. This is followed by discussions of errors related to multiple solutions in Section V and to vertical profiles in Section VI. In Section VII, the HB-DFR algorithm as a fully or partially single-frequency algorithm is explained. It is applied to the synthetic dataset with measured radar reflectivity factors smaller than the minimum detection level being masked. The summary and conclusions are given in Section VIII.

II. SYNTHETIC DATASET

To test the HB-DFR algorithm, a synthetic dataset is produced from the PR standard product in version 7. The synthetic dataset has vertical profiles of the measured radar reflectivity factor [denoted by Z_m (in mm^6 m^{-3})] at 13.8GHz and 35.5GHz. The PR frequency (13.8 GHz) is used instead of the KuPR frequency (13.6 GHz) to ease production of the synthetic dataset. This minor difference in frequency does not significantly affect the results obtained. The vertical resolution of the synthetic dataset [denoted by L (km)] is 0.25 km, but oversampled data are not produced. A profile with N range bins is presented in Fig. 2. Here the range bin number increases in the downward direction; the highest range bin is range bin 1 and the lowest range bin is range bin N. The r axis is taken along the radar beam, and r gives the distance from the radar. Let r equal r_{i-1} at the top of range bin i and r_i at the bottom of range bin i. The phase (liquid / melting / solid) of range bin is determined according to the PR standard product. DSD parameters are not stored in the PR standard product, but they can be calculated from the effective radar reflectivity factor [denoted by Z_e (in mm^6 m^{-3})] and the specific attenuation [denoted by k (in decibels per kilometer)] as follows. The value of k is also not stored in the standard product, but can be calculated by the k-Z relation shown in

$$k(r) = \varepsilon \alpha_0(r) Z_e(r)^{\beta} \tag{1}$$

where α_0 and β are parameters dependent on the precipitation type. α_0 is vertically variable, but β is constant. The values of α_0 at some range bins (termed nodes) and β are given in the standard product (Table I). The

nodes are defined by referring to a bright band (if it exists) and air temperature as illustrated in Fig. 3. α_0 at the other range bins can be calculated by linear interpolation. ε is termed the *k*-adjustment factor in this paper and its value is given in the standard product.

A. DSD at Liquid Phase Range Bins

At liquid phase range bins, according to the PR standard algorithm, the DSD is assumed to follow the function given in

$$N(D) = N_w f(D;\mu,D_m) \tag{2-1}$$

$$f(D;\mu,D_m) \equiv \frac{6(\mu+4)^{\mu+4}}{4^4\Gamma(\mu+4)}\left(\frac{D}{D_m}\right)^{\mu}\exp\left[\frac{-(\mu+4)D}{D_m}\right] \tag{2-2}$$

where D (in millimeters) is the diameter of a precipitation particle, and $N(D)$ (in m^{-3} mm^{-1}) is the number density. N_w (in m^{-3} mm^{-1}) and D_m (in millimeters) are the DSD parameters to be retrieved. The third DSD parameter μ is fixed to be 3 throughout this paper. With this assumption, Z_e (in mm^6 m^{-3}) and k (in decibels per kilometer) are written as functions of the DSD parameters as shown in

$$Z_e = N_w F(D_m) \tag{3-1}$$

$$F(D_m) \equiv \frac{\lambda^4}{\pi^5}\left|\frac{n_w{}^2+2}{n_w{}^2-1}\right|^2 \int_{D=0}^{\infty}\sigma_b(D) f(D;\mu,D_m)dD \tag{3-2}$$

where σ_b is the backscattering cross section (in square millimeters), λ is the wavelength of the microwave (in centimeters), and n_w is the refractivity index of water in liquid phase at 0^oC.

$$k = N_w G(D_m) \tag{4-1}$$

$$G(D_m) \equiv \frac{0.01}{\ln(10)}\int_{D=0}^{\infty}\sigma_e(D) f(D;\mu,D_m)dD \tag{4-2}$$

where σ_e is extinction cross section (in square millimeters).

By dividing Eq. (4-1) by Eq. (3-1), k/Z_e is found to be a function of D_m.

$$k / Z_e = G(D_m)/F(D_m) . \quad (5)$$

As shown in Fig. 4, k/Z_e at node D (liquid phase, 0^oC) is a monotonic decreasing function of D_m as long as D_m takes realistic values. This means that D_m can be retrieved uniquely from k/Z_e. Once D_m is derived, N_w can be calculated by substituting D_m into (3) or (4). Z_e and k at 35.5 GHz are calculated from the DSD parameters using (3) and (4), respectively.

The precipitation rate R (in millimeters per hour) is calculated from the DSD parameters as shown in

$$R = N_w H(D_m) \quad (6\text{-}1)$$

$$H(D_m) \equiv 0.6\pi \times 10^{-3} \int_{D=0}^{\infty} V(D) D^3 f(D; \mu, D_m) dD \quad (6\text{-}2)$$

where $V(D)$ (in meters per second) denotes a falling velocity function and is given in the following equation according to Gunn and Kinzer [10].

$$V(D) = 4.854 \times D \times \exp(-0.195D) \quad (7)$$

For all liquid phase range bins, particle temperature (denoted by T) is set to be 0^oC in order to calculate σ_b and σ_e, as their dependence on temperature is negligible. Dependence of the falling velocity on air pressure is also neglected, and (7) is always used for liquid phase range bins. As long as the same $V(D)$ is used in the retrieval algorithm, this simplified assumption does not affect the performance of the retrieval algorithm.

B. DSD at Solid and Melting Phase Range Bins

At solid and melting phase range bins, according to Awaka's model [11],[12], the DSD is simulated to follow (2) when all the particles melt into the liquid phase with non-coalescence and non-breakup assumption. This assumption is written as shown in

$$N(D)V(D)dD = N_s(D_s)V_s(D_s)dD_s \quad (8\text{-}1)$$

$$D^3 = \rho_s D_s^3 \quad (8\text{-}2)$$

where the variables with subscripts s denote the solid and melting phases, and variables without subscripts

indicate post melting. ρ_s (in grams per cubic centimeters) denotes the density of a solid and melting phase particle. V_s (in meters per second) depends on ρ_s as shown in

$$V_s = 3.3 \times \rho_s^{0.5} \qquad (\rho_s \le 0.05) \tag{9-1}$$

$$V_s = 8.8 \times (0.1 D_s \rho_s)^{0.5} \qquad (0.05 \le \rho_s \le 0.3) \tag{9-2}$$

$$V_s = \frac{(V - V_{s0.3})(\rho_s^{1/3} - 0.3^{1/3})}{(1 - 0.3^{1/3})} + V_{s0.3} \qquad (0.3 \le \rho_s \le 1.0) \tag{9-3}$$

where $V_{s0.3}$ is V_s with ρ_s=0.3 and is given by (9-2). V is given by (7).

The refractivity index of solid and melting phase particles (denoted by n_s) is determined as follows:

$$\frac{n_s^2 - 1}{n_s^2 + U} = P_w \frac{n_w^2 - 1}{n_w^2 + U} + P_i \frac{n_i^2 - 1}{n_i^2 + U} \tag{10}$$

where P_w is the volumetric ratio of liquid water to the particle and P_i is the volumetric ratio of solid water to the particle. U is a form factor. n_i is the dielectric constant of ice, and n_w and n_i depend on T. According to the PR standard algorithm, T, P_w, P_i, ρ_s, and U are given for the nodes as shown in Table I.

Using the above settings, $F(D_m)$ and $G(D_m)$ can be calculated for the nodes. For range bins between the nodes, $F(D_m)$ and $G(D_m)$ are linearly interpolated for the distance r. For range bins above node A, $F(D_m)$ and $G(D_m)$ are identical to those at node A. In the same way in liquid phase range bins, N_w and D_m are calculated from k and Z_e at 13.8 GHz, and k and Z_e at 35.5 GHz are then calculated from N_w and D_m.

C. Simulation of Z_m at Range Bins

As the DSD is assumed to be uniform in a range bin, $Z_e(r)$ and $k(r)$ are constant in the range bin. The constant values at range bin i are denoted as $\langle Z_e \rangle_i$ and $\langle k \rangle_i$, respectively. However, $Z_m(r)$ is not constant in the range bin. $Z_m(r)$ at the top of range bin i and the bottom of range bin i are given as shown in

$$\mathrm{dB}Z_m(r_{i-1}) = \mathrm{dB}\langle Z_e \rangle_i - 2\sum_{j=1}^{i-1} \langle k \rangle_j L \tag{11}$$

$$\mathrm{dB}Z_m(r_i) = \mathrm{dB}\langle Z_e \rangle_i - 2\sum_{j=1}^{i} \langle k \rangle_j L \tag{12}$$

where the prefix "dB" indicates that the variable is given at the decibel scale as dBZ=10log$Z$. j is a dummy parameter of i. Measured radar reflectivity factor at range bin i is denoted by $\langle Z_m \rangle_i$ and is assumed to be given as shown in

$$\mathrm{dB}\langle Z_m \rangle_i \equiv \mathrm{dB}\langle Z_e \rangle_i - 2\sum_{j=1}^{i-1} \langle k \rangle_j L - 0.5 \times 2\langle k \rangle_i L \tag{13}$$

The third term on the right hand side of (13) represents the "internal attenuation", which is caused by precipitation particles inside range bin i.

A synthetic dataset are produced from 489 PR orbits observed in July 2001. Because of limited computer resources, no more than 10,000 precipitating pixels are selected from each orbit. At each pixel, a series of continuous precipitating range bins is taken. Precipitating range bins separated from lower precipitating range bins are neglected in producing the synthetic dataset.

III. Dual-frequency Algorithm

When dual-frequency measurements are available at all range bins in a profile, the HB-DFR algorithm can be fully applied as a dual-frequency algorithm. The framework of the HB-DFR algorithm as a dual-frequency algorithm is shown in Fig. 5. Z_m, α_0, and β are given at each range bin and at each frequency. Initially, the k-adjustment factor is arbitrarily given at each range bin and at each frequency. Although the k-adjustment factor is vertically constant in the PR standard algorithm, it can vary between range bins in this dual-frequency algorithm, allowing higher degrees of freedom in the DSD. Moreover, the k-adjustment factor can be different for KuPR and KaPR.

The procedure can be divided into steps (i) to (iv). At each frequency, the vertical profile of Z_e is derived

using the HB method [steps (i) and (ii)]. At each range bin, the DSD parameters (N_w, D_m) are derived from the dual-frequency Z_e values using the DFR method [step (iii)]. At each range bin and at each frequency, the *k*-adjustment factor is calculated from the derived (N_w, D_m) by (1), (3), and (4) [step (iv)]. With the updated *k*-adjustment factors, steps (i) to (iv) are executed again. In this way, steps (i) to (iv) are iteratively applied to optimize the *k*-adjustment factors. Details of the HB method and the DFR method are described below.

A. HB Method

Here, the HB method is briefly reviewed. When a *k*-*Z* relation is assumed as in (1), $Z_e(r)$ is analytically solved as shown in

$$Z_e(r) = \frac{Z_m(r)}{\left[1-\varsigma(r)\right]^{1/\beta}} \tag{14-1}$$

$$\varsigma(r) \equiv 0.2\times\ln(10)\times\beta\int_0^r \varepsilon\alpha_0(s)Z_m(s)^\beta ds \tag{14-2}$$

where *s* is a dummy parameter of *r*.

In reality, $<Z_m>_i$ (i=1,...,N) is given instead of $Z_m(r)$, so the HB method needs to be applied in its discrete form. The discrete form of Eq. (14-2) at $r=r_i$ is given as shown in

$$\varsigma(r_i) = 0.2\times\ln(10)\times\beta\sum_{j=1}^{i}\varepsilon_j\alpha_{0j} < Z_m >_j^{\beta} L\frac{e^{\kappa_j}-e^{-\kappa_j}}{2\kappa_j} \tag{15-1}$$

$$\kappa_j \equiv 0.1\times\ln(10)\times < k >_j L \tag{15-2}$$

where α_{0j} and ε_j respectively denote α_0 and ε at range bin *j*. The last factor of Eq. (15-1) appears as Z_m does not linearly change with *r* in each range bin. This factor is close to 1 when attenuation is weak, but it becomes large and cannot be neglected for heavy precipitation. To calculate $\varsigma(r_i)$, the following iterative procedure is applied.

[1] $<k>_i$ is assumed to be zero.

[2] $\varsigma(r_i)$ is calculated by (15).

[3] $<k>_i$ can be calculated from the following equation, the second equality of which is derived from (14-1).

$$< k >_i = \frac{1}{2L}\left[10\log_{10}\frac{Z_m(r_{i-1})/Z_e(r_{i-1})}{Z_m(r_i)/Z_e(r_i)}\right] = \frac{1}{2L}\left\{10\log_{10}\frac{\left[1-\varsigma(r_{i-1})\right]^{1/\beta}}{\left[1-\varsigma(r_i)\right]^{1/\beta}}\right\} \tag{16}$$

[4] Return to [2] with the updated $<k>_i$; Repeat [2] and [3] until $<k>_i$ converges.

[5] $<k>_i$ and $\zeta(r_i)$ are finally determined, and $<Z_e>_{\underline{i}}$ is calculated from (17), the third equality of which can be derived from (12) and (13).

$$< Z_e >_i = Z_e(r_i) = \frac{Z_m(r_i)}{\left[1-\varsigma(r_i)\right]^{1/\beta}} = \frac{< Z_m >_i \times 10^{0.1<k>_i L}}{\left[1-\varsigma(r_i)\right]^{1/\beta}} . \tag{17}$$

The above process is applied from range bin 1 to N sequentially, therefore $\zeta(r_{i-1})$ is known in calculating (16). If $\zeta(r_i)$ becomes larger than 1, k-adjustment factors for all range bins are set smaller and the above process is applied again from range bin 1.

For KuPR, α_0 and β are given according to the PR standard algorithm [11]. For KaPR, α_0 is set to be 10 times as large as that for KuPR, and β is set to be the same as that for KuPR.

B. DFR Method

Once Z_e's are given at both frequencies, DFR defined in (18) can be calculated.

$$\mathrm{DFR} \equiv \mathrm{dB}Z_e^a - \mathrm{dB}Z_e^u = 10\log_{10} F^a(D_m) - 10\log_{10} F^u(D_m) \tag{18}$$

where superscript a (u) indicates that the value is for KaPR (KuPR). DFR as a function of D_m is shown in Fig. 6 for the various nodes. At nodes A, B, and C (solid and melting phase; the physical properties are given in Section II and Table I), DFR is a monotonic decreasing function; therefore, D_m can be uniquely determined. When D_m is derived, N_w can be calculated by (3). In this way, DSD parameters (D_m and N_w) are retrieved by the DFR method. At node D (liquid phase, 0^oC), DFR takes a local maximum, and the value of D_m at which DFR reaches the local maximum is denoted by $D_{m,s}$. In the case of μ=3, $D_{m,s}$ = 1.01 mm. When a given DFR is larger than 0 dB, there are two possible D_m values. In this case, the larger D_m is selected. When a given

DFR is smaller than 0 dB, D_m is uniquely determined.

IV. Testing and Evaluation

The HB-DFR algorithm is applied to the synthetic dataset. In this section, two experiments are conducted: the standard experiment (STD) and the ideal experiment (IDL). In these two experiments, to fully apply the HB-DFR algorithm as a dual-frequency algorithm, the minimum detection level of Z_m (18 dBZ in normal scans of the DPR) is not considered; Z_m's smaller than 18 dBZ are input as "measured" in the two experiments.

In the STD, the *k*-adjustment factor is initially set to be 1 at all range bins and at both frequencies. Steps (i) to (iv) are preformed 100 times. In the IDL, the true value of the *k*-adjustment factor is determined initially at all range bins and at both frequencies, and steps (i) to (iv) are performed once only. To see how errors in the *k*-adjustment factor affected the precipitation rate estimates, the IDL and STD results are compared. Precipitation rates at the lowest range bin of each profile are evaluated, because they are often used as near surface precipitation rates and are affected by accumulated errors in the upper range bins. Here and later in this paper, "precipitation rate" indicates the precipitation rate at the lowest range bin, unless the range bin number is otherwise specified.

A. IDL

Fig. 7 shows the evaluation for the IDL. Precipitation rates estimated by the HB-DFR algorithm (called "estimates") are compared with those directly calculated from the DSD of the synthetic dataset (called "truths"). In this figure, both axes are in logarithmic scale. The average of the estimates is shown for all pixels and for each category of the thickness [denoted by TOL (in kilometers)] of the liquid phase range bins; the categories are TOL = 0 km, 0 km < TOL <= 1 km, 1 km < TOL <= 2 km, 2 km < TOL <= 3 km, 3 km < TOL <= 4 km, 4 km < TOL <= 5 km, and 5 km < TOL. A two-dimensional histogram of the estimates and the

truths is also shown for all pixels.

The estimates are very close to the truths, except for "very heavy precipitation" (above 30 mm h^{-1}) and for "light precipitation" (below 1 mm h^{-1}). As shown in Fig. 8(a),(b), KuPR PIA is accurately retrieved but KaPR PIA is underestimated for very heavy precipitation. For very heavy precipitation, $\zeta(r_N)$ is very close to 1 at KaPR, but we tend to use smaller *k*-adjustment factor in avoiding numerical divergence so that $\zeta(r_N)$ is likely to be underestimated.

For light precipitation, the HB method has no problems but the DFR method selects an incorrect D_m. As shown in Fig. 8(c), D_m at the lowest range bin is overestimated because a D_m larger than $D_{m,s}$ is always selected in the DFR method, whereas the average of the true D_m is smaller than $D_{m,s}$. As shown in Fig. 7, for the category of TOL = 0 km (the phase at the lowest range bin is solid or melting), the precipitation rate is not underestimated. This is because the DFR method has no multiple solutions for solid and melting phase range bins. As shown in Fig. 8(c), D_m is also overestimated for very heavy precipitation, but this is caused by the inappropriate KaPR Z_e derived by the HB method, not by multiple solutions in the DFR method.

Fig. 8(d) shows the KuPR *k*-adjustment factor at the lowest range bin. For light and very heavy precipitation, the *k*-adjustment factor estimated in step (iv) is different from that assumed in step (i). This suggests that the precipitation rate estimates are not reliable when the *k*-adjustment factor does not converge.

B. STD

Evaluations are also made for the STD. The precipitation rates that are evaluated are shown in Fig. 9. Fig. 10 shows the PIAs for KuPR and KaPR, D_m at the lowest range bin, and the KuPR *k*-adjustment factor at the lowest range bin. Compared with the IDL, the STD generated larger errors in the precipitation rates (Fig. 9). For "heavy precipitation" (above 10 mm h^{-1}), PIAs are underestimated at both frequencies [Fig. 10(a),(b)] and precipitation rates are more substantially underestimated than in the IDL. The underestimation for heavy precipitation is more severe when the TOL category is larger (Fig. 9). The reason for this is explained by the

examination of vertical profiles in Section VI. For light precipitation, an incorrect D_m is likely to be selected [Fig. 10(c)], and precipitation rates are underestimated as is in the IDL. For "medium precipitation" (between 1 and 10 mm h^{-1}), the estimates are generally close to the truths, although they are not as accurate as the IDL. In the synthetic dataset, nearly half of the total amount of precipitation occurred as medium precipitation. The result supports the potential of the HB-DFR algorithm for medium precipitation.

While errors in the IDL resulted from the use of the HB and DFR methods, errors in the STD are also caused by the *k*-adjustment factor. In the 100th iteration of the STD, the assumed *k*-adjustment factor (the estimates after the 99th iteration) is different from the truth particularly for light and heavy precipitation [Fig. 10(d)]. The *k*-adjustment factor after the 100th iteration is almost the same as after the 99th iteration. This indicates that the *k*-adjustment factor largely converges by the 100th iteration, but sometimes to an incorrect value. This can be explained by the fact that there are multiple solutions in the HB-DFR algorithm as will be shown in Section V.

V. Multiple Solutions

A. *Multiple Solutions in a Dual-frequency Forward Retrieval Algorithm*

Here, the theory of multiple solutions in a dual-frequency forward retrieval algorithm given in Seto and Iguchi [6] is summarized. A forward retrieval algorithm solves the DSD from range bin 1 to range bin *N*. Before the DSD at range bin *i* is solved, attenuation is corrected for range bins 1 to (*i*-1), or $\langle Z_f \rangle_i$ as defined in the following equation can be calculated at both frequencies.

$$\mathrm{dB}\left\langle Z_f \right\rangle_i \equiv \mathrm{dB}\left\langle Z_m \right\rangle_i + 2\sum_{j=1}^{i-1}\left\langle k \right\rangle_j L \quad . \tag{19}$$

$\langle Z_f \rangle_i$ is not equal to $\langle Z_e \rangle_i$, as the internal attenuation is not corrected in $\langle Z_f \rangle_i$.

From (3), (4), (13), and (19), the following equation is derived.

$$\mathrm{dB}\left\langle Z_f \right\rangle_i = \mathrm{dB}\left\langle Z_e \right\rangle_i - \left\langle k \right\rangle_i L = \mathrm{dB}N_{w,i} + \mathrm{dB}F(D_{m,i}) - N_{w,i}G(D_{m,i})L \tag{20}$$

where $N_{w,i}$ and $D_{m,i}$ are N_w and D_m at range bin i, respectively. $<Z_\mathrm{f}>_i$ is a function of $N_{w,i}$ and $D_{m,i}$ and independent of other range bins, while $<Z_\mathrm{m}>_i$ depends not only on $N_{w,i}$ and $D_{m,i}$ but on DSD parameters at other range bins. Therefore, it is easier to derive $N_{w,i}$ and $D_{m,i}$ from $<Z_\mathrm{f}>_i$ than from $<Z_\mathrm{m}>_i$. In the remainder of this subsection, the 0^oC liquid phase is assumed for range bin i, and the subscript i is omitted for simplicity.

In Fig. 11, D_m is shown as the horizontal axis and the difference in $\mathrm{dB}<Z_f>$ at the two frequencies (denoted by $\mathrm{dB}<Z_f>^\delta$ as defined in the following equation) is shown by the vertical axis.

$$\mathrm{dB}\left\langle Z_f \right\rangle^\delta \equiv \mathrm{dB}\left\langle Z_f \right\rangle^a - \mathrm{dB}\left\langle Z_f \right\rangle^u = dBF^a(D_m) - dBF^u(D_m) - N_w L\left[G^a(D_m) - G^u(D_m)\right] \tag{21}$$

When a set of D_m and $\mathrm{dB}<Z_f>^\delta$ is given, N_w is uniquely determined. Therefore, except for the gray region with negative N_w, any point on this plane corresponds to a set of DSD parameters.

The contours in Fig. 11(a) represent $\mathrm{dB}N_w$ and the precipitation rates. Contours are also drawn for $\mathrm{dB}<Z_f>^\mathrm{u}$ and $\mathrm{dB}<Z_f>^\mathrm{a}$ in Fig. 11(b). There are two crossing points for a given set of $\mathrm{dB}<Z_f>^\mathrm{u}$ and $\mathrm{dB}<Z_f>^\mathrm{a}$, which suggests that there are two possible solutions for the DSD per range bin in dual-frequency forward retrieval algorithms. According to Seto and Iguchi [6], the plane can be categorized into four types (except for the gray region), as shown by the four different background colors. If the DSD of one solution is in type-0 / type-1 / type-2 / type-3, the DSD of the other solution is in type-1 / type-0 / type-3 / type-2. In type-0, D_m is smaller than $D_{m,s}$. D_m in type-2 is larger than the corresponding D_m in type-3. Detailed explanation about the four types are given in [6].

B. Multiple Solutions in the HB-DFR Algorithm

In the DFR method, no type-0 DSDs are selected. If the true solution is in type-0, it is never selected in the HB-DFR algorithm. Conversely, if the true solution is in type-1, it is easily selected. If the true solution is in type-2 or type-3, the initial assumption of the k-adjustment factor may determine whether the HB-DFR

algorithm selects the type-2 or type-3 DSD. In Fig. 11(c), contours are shown for the KuPR and KaPR *k*-adjustment factors in the case of stratiform precipitation. Fig. 11(d) is the same as Fig. 11(c), but in the case of convective precipitation. The initial *k*-adjustment factor assumed for the STD (ε=1 at both frequencies) corresponds to type-1 DSD or type-2 DSD with the exception of convective precipitation heavier than 50 mm h^{-1}. This suggests that type-2 DSD is much more likely to be selected than type-3 DSD.

Fig. 12 shows the evaluation of precipitation rates for pixels which do not have type-0 and type-3 DSDs. Nearly 30 % of all pixels satisfy this condition, or have only type-1 and type-2 DSDs. The underestimation for light precipitation disappears in both the IDL and STD, when type-0 DSDs are excluded. The underestimation for heavy precipitation is also alleviated as type-3 DSDs are excluded. Overall, the bias ratios for pixels without type-0 and type-3 DSDs are -2.525% in the IDL and -12.931% in the STD and are better than -6.315% and -35.229%, respectively, for all pixels.

VI. Vertical Profile

In a forward retrieval algorithm, errors transfer and expand in going forward (downward). Vertical profiles are examined to see how errors transfer to lower range bins in the STD. In Fig. 13, “averaged” vertical profiles are shown for Z_m (truths), Z_e (truths and estimates from the STD), and precipitation rates (truths and estimates from the STD). Fig. 13(a)-(c) represent vertical profiles with a bright band. The vertical axis indicates the particle temperature for solid phase range bins, relative location in a bright band for melting phase range bins, and the distance from the bottom of the bright band for liquid phase range bins. At each level of the vertical axis, data are averaged except for non-precipitating range bins; therefore, the number of samples can be different at different levels. Fig. 13(d)-(f) represent vertical profiles without bright bands. The vertical axis indicates the particle temperature for solid phase range bins and the distance from the top of the liquid phase (not necessarily equal to the freezing level) for liquid phase range bins.

At solid and melting phase range bins, almost no errors are seen in Z_e and precipitation rates, because the

DFR method generally does not have multiple solutions at these range bins. However, it should be noted that $F(D_m)$ and $G(D_m)$ are set accurately in this study. The inappropriate setting of $F(D_m)$ and $G(D_m)$ may cause errors at these range bins. At liquid phase range bins, errors are observed in Z_e and precipitation rates, which expand in going downward. This is likely the reason why the precipitation rate is more substantially underestimated when the TOL is larger.

VII. Application to Partial Single-frequency Profiles

In previous sections, the HB-DFR algorithm is applied fully as a dual-frequency algorithm. In this section, we explain the modification of the HB-DFR algorithm to be applied fully or partially as a single-frequency algorithm.

For KuPR single-frequency measurement [pixel type (A)], a simplified version of the HB-DFR algorithm can be applied. The framework of the KuPR algorithm is shown in Fig. 14(a). Compared with the HB-DFR algorithm fully as a dual-frequency algorithm (Fig. 5), the HB method for KaPR [step (ii)] and the update of *k*-adjustment factor [step (iv)] are omitted. Instead of the DFR method [step (iii)], DSD parameters are retrieved from the ratio of k and Z_e as applied in producing the synthetic dataset [step (iii')]. Similarly, the framework of an algorithm for KaPR single-frequency measurement [pixel type (B)] is shown in Fig. 14(b); Steps (ii) and (iii') are applied.

Even for dual-frequency measurement [pixel type (C)], the HB-DFR algorithm cannot be always applied fully as a dual-frequency algorithm, because Z_m's smaller than 18 dBZ is not available in actual DPR measurements. KaPR measurement is subject to precipitation attenuation and often lacks echoes at lower range bins. Below, we explain the procedure how the HB-DFR algorithm is applied when some Z_m's are masked, and test the HB-DFR algorithm with the synthetic dataset by masking Z_m's smaller than 18 dBZ.

A. The Procedure of the HB-DFR Algorithm partially as a single-frequency algorithm

Even if some Z_m's are masked, the HB-DFR algorithm is performed basically in the same way as explained in section 3, but there are some exceptions. In the HB method, if Z_m is smaller than 18 dBZ at range bin i, Z_e is assumed to be equal to Z_e of range bin (i-1). However, if all Z_m's are smaller than 18 dBZ between range bins 1 to i, Z_e at range bin i cannot be assumed.

The k-adjustment factor is updated by the DFR method only at range bins where the Z_m's are larger than 18 dBZ at both frequencies. As shown in Table II, an index is selected from which the DSD is retrieved at range bin i depending on the conditions in Z_{m} (Z_m is larger than 18 dBZ at range bin i, Z_m is smaller than 18 dBZ at range bin i but some Z_{m}'s are larger than 18 dBZ at range bins 1 to i-1, Z_m's are smaller than 18dBZ at all range bins 1 to i). In some cases, the DSD is retrieved from k/Z_{e} at either frequency as in the fully single-frequency algorithm. As k/Z_e is not a monotonic function of D_m for KaPR (figures not shown),the smaller D_m is selected, if there are two possible solutions of D_m. If all Z_{m}'s are smaller than 18dBZ at range bins 1 to i at both frequencies, the DSD and precipitation rates cannot be retrieved at range bin i and above. If all Z_{m}'s are masked from range bin 1 to N at either frequency, the algorithm reduces to a fully single-frequency algorithm. Here, the dual-frequency algorithm, the fully single-frequency algorithms, and the partial single-frequency algorithm are given in common framework.

B. Test and Results

The HB-DFR algorithm is applied to the synthetic dataset with masking Z_{m}'s smaller than 18 dBZ. This experiment is called the Minimum Detection Level experiment (MDL). If all Z_m's at both frequencies are masked in a pixel, the pixel cannot be used in the MDL. For this reason almost 10% of all the pixels used in the STD are not used in the MDL.

Precipitation rates estimated by the MDL are evaluated (Fig. 15). The lowest range bin and the TOL are defined by including masked range bins, and hence they are the same for the MDL and STD. The ratio of bias

is -19.344 % in the MDL, and is better than -35.229 % in the STD (-35.111 % in the STD for the pixels which are used in the MDL). In the MDL, substantial underestimation of heavy precipitation is alleviated. Whereas larger biases are found for larger TOL in the STD, this is not true for the MDL. Some precipitation rates are overestimated in the MDL particularly for light precipitation, as shown in the two-dimensional histogram, while such overestimates are rarely seen in the STD. These differences between the MDL and STD are discussed by examining vertical profiles.

C. *Vertical Profiles*

"Averaged" vertical profiles of Z_e and precipitation rates estimated from the MDL are shown in Fig. 16. Vertical profiles of Z_m, true Z_e, and true precipitation rates are also shown, but are slightly different from those shown in Fig. 13 because some profiles are not used in the MDL. At lower liquid phase range bins, the KaPR Z_m sometimes becomes smaller than 18 dBZ due to attenuation. Whereas errors in Z_e become larger at lower range bins in the STD, this is not evident in the MDL. This is likely because a vertically constant Z_e is assumed when Z_m's are masked. Consequently, underestimation in Z_e is alleviated in the MDL. By avoiding the use of underestimated Z_e, the precipitation rates are better estimated in the MDL than in the STD.

At solid phase range bins, Z_e is slightly overestimated in the MDL. At the -20^{o}C level (node A and above), the KaPR true Z_e tends to be higher than that at lower solid phase range bins for this synthetic dataset. In this case, by assuming vertical constancy in Z_e, Z_e is overestimated at lower solid phase range bins. Similar phenomenon may occur at liquid phase range bins when the precipitation rate is light. If true Z_e decreases with depth and Z_m is masked, Z_e is overestimated. This may cause an overestimation for light precipitation.

VIII. Summary and Conclusions

This study proposes the HB-DFR algorithm for the GPM/DPR. When the HB-DFR algorithm is applied as

a fully dual-frequency algorithm, it has multiple solutions in a similar manner to other dual-frequency forward retrieval algorithms. The HB-DFR algorithm is likely to select a solution with a smaller precipitation rate, so the performance is satisfactory for medium precipitation but is not good for heavy precipitation. As with other forward retrieval algorithms, errors transfer and expand in the downward direction. Vertical profiles suggest that these errors are largely caused by liquid phase range bins rather than solid and melting phase range bins. Therefore, biases in precipitation rates at the lowest range bin are larger when liquid phase range bins are thicker.

The HB-DFR algorithm can be easily switched to a single-frequency retrieval algorithm at a range bin where a measurement at one of the two frequencies is not available. This is an advantage over dual-frequency algorithms proposed previously and we believe that the HB-DFR algorithm is suitable for use as part of the DPR standard algorithm. At a range bin where the KaPR Z_m is smaller than the minimum detection level of 18 dBZ because of strong attenuation, information from KuPR only is used, which avoided the substantial underestimation inherent in dual-frequency forward retrieval algorithms.

Throughout this study, no measurement errors in Z_m are considered, and $F(D_m)$ and $G(D_m)$ are provided accurately. However, these ideal conditions cannot be expected under real operation. An operational retrieval algorithm for the DPR should be more robust so that it does not cause large errors even if Z_m has some measurement errors and the tables are not provided accurately. SRT is necessary to make retrieval algorithms more robust. We are going to develop an HB-DFR-SRT algorithm in future work.

REFERENCES

[1] T. Iguchi, T. Kozu, R. Meneghini, J. Awaka, and K. Okamoto, “Rain-profiling algorithm for the TRMM Precipitation Radar,” *J. Appl. Meteorol.*, vol. 39, no. 12, pp. 2038-2052, Dec. 2000.

[2] T. Iguchi, T. Kozu, J. Kwiatkowski, R. Meneghini, J. Awaka, and K. Okamoto, “Uncertainties in the rain profiling algorithm for the TRMM Precipitation Radar,” *J. Metorol. Soc. Jpn.*, vol. 87A, pp. 1-30, Mar. 2009.

[3] W. Hitschfeld and J. Bordan, “Errors inherent in the radar measurement of rainfall at attenuating wavelengths,” *J. Meteorol.*, vol. 11, pp. 58-67, 1954.

[4] R. Meneghini, H. Kumagai, J. R. Wang, T. Iguchi, and T. Kozu, “Microphysical retrievals over stratiform rain using measurements from an airborne dual-wavelength radar-radiometer,” *IEEE Trans. Geosci. Remote Sens.*, vol. 35, no. 3, pp. 487-506, May 1997.

[5] R. Mardiana, T. Iguchi, and N. Takahashi, “A dual-frequency rain profiling method without the use of a surface reference technique,” *IEEE Trans. Geosci. Remote Sens.*, vol. 42, no. 10, pp. 2214-2225, Oct. 2004.

[6] S. Seto and T. Iguchi, “Applicability of the iterative backward retrieval method for the GPM Dual-frequency Precipitation Radar,” *IEEE Trans. Geosci. Remote Sens.*, vol. 49, no. 6, pp. 1827-1838, Jun. 2011.

[7] C. R. Rose and V. Chandrasekar, “A systems approach to GPM dual-frequency retrieval,” *IEEE Trans. Geosci. Remote Sens.*, vol. 43, no. 8, pp. 1816-1826, Aug. 2005.

[8] N. B. Adhikari, T. Iguchi, S. Seto, and N. Takahashi, “Rain retrieval performance of a dual-frequency precipitation radar technique with differential-attenuation constraint,” *IEEE Trans. Geosci. Remote Sens.*, vol. 45, no. 8, pp. 2612-2618, Aug. 2007.

[9] C. R. Rose and V. Chandrasekar, “Extension of GPM dual-frequency iterative retrieval method with DSD-profile constraint,” *IEEE Trans. Geosci. Remote Sens.*, vol. 44, no. 2, pp. 328-335, Feb. 2006.

[10] R. Gunn, G. G. Kinzer, “The terminal velocity of fall for water droplets in stagnant air,” *J. Meteorol.*, vol. 6, pp. 243-248, 1949.

[11] J. Awaka, Y. Furuhama, M. Hoshiyama, and A. Nishitsuji, “Model calculations of scattering properties of spherical bright-band particles made of composite dielectrics,” *J. Radio Res. Lab.*, vol. 32, pp 73-87, 1985.

[12] M. Thurai, H. Kumagai, T. Kozu, and J. Awaka, “Effects of incorporating a brightband model in a downward-looking radar rainfall retrieval algorithm,” *J. Atmos. Ocean. Technol.*, vol. 18, no. 1, Jan. 2001.

[13] T. Kozu, T. Iguchi, T. Shimomai, and N. Kashiwagi, “Raindrop size distribution modeling from a statistical rain parameter relation and its application to the TRMM Precipitation Radar rain retrieval algorithm,” *J. Appl. Meteorol. Climatol.* vol. 48, no. 4, Apr. 2009.

Shinta Seto (M'10) received B.E., M.E., and Ph.D. degrees from the University of Tokyo, Japan, in 1998, 2000, and 2003, respectively.

From 2003 to 2006, he was with the National Institute of Information and Communications Technology (formerly the Communications Research Laboratory), Japan, as a Postdoctoral Researcher, where he worked on the development of spaceborne dual-frequency precipitation radar. Since 2006, he has been with the Institute of Industrial Science, the University of Tokyo. His current research interests include precipitation retrieval using microwave remote sensing and its application to water cycle studies.

Toshio Iguchi (M'97) received a B.Sc. degree from Hokkaido University, Japan, in 1976, a M.Sc. degree from the University of Tokyo, Japan, in 1978, and a Ph.D. degree from York University, Canada, in 1983.

Since 1985, he has been with the National Institute of Information and Communications Technology (formerly the Communications Research Laboratory), Japan. He visited the NASA/Goddard Space Flight Center, MD, from 1991 to 1994, performing the US–Japan collaborative experiment for measuring rain using airborne radar. Since then, he has focused primarily on issues related to the remote sensing of precipitation from space.

Taikan Oki received B.E., M.E., and Ph.D. degrees from the University of Tokyo, Japan, in 1987, 1989, and 1993, respectively. Before he was assigned to be a professor at IIS, The University of Tokyo in 2006, he stayed as a Visiting Scientist at NASA/GSFC, USA, for 1995-97, as an Associate Professor at the Research Institute for Humanity and Nature in Kyoto, Japan, for 2001-03, and as a Deputy Director for Environment and Energy at the Council for Science and Technology Policy, Cabinet Office of

Japan, for 2005-06. He is one of the coordinating lead authors for the fifth assessment report of IPCC. He got many awards including the Biwako Prize for Ecology in 2011, the Japan Academy Medal from The Japan Academy, and JSPS PRIZE from Japan Society for the Promotion of Science in 2008. His research interests within the field of global hydrology and world water resources including the virtual water trade and water footprint, impacts of climate change on hydrological extremes, and integrated water resources managements in Asian Monsoon regions.

TABLE I

SETTINGS OF PHASE AND PARAMETERS AT THE NODES. NODES A, B, C, AND D ARE DESIGNATED BY THE PR STANDARD ALGORITHM (ILLUSTRATED IN FIG. 3). α_0 AND β ARE DEPENDENT ON PRECIPITATION TYPES: STRATIFORM INDICATED BY [S] AND CONVECTIVE INDICATED BY [C].

node	phase	T [^{o}C]	P_w	P_i	ρ_s [g cm^{-3}]	U	α_0 for KuPR [x 10^{-4}]	β
node A	solid	-20	0.000	0.109	0.100	2.0	0.3124 [S] 0.4814 [C]	0.78069 [S] 0.75889 [C]
node B	melting	0	0.017	0.123	0.130	3.4	1.2651 [S]	
(between B and C)	melting	0	0.044	0.180	0.210	8.7	3.1409 [S]	
node C	melting	0	0.170	0.263	0.412	140	5.0167 [S]	
(between C and D)	melting	0	0.380	0.257	0.616	140	4.0639 [S]	
node D	liquid	0	1.000	0.000	1.000		3.1110 [S] 4.2864 [C]	

TABLE II

INDICES FROM WHICH THE DSD IS RETRIEVED AT RANGE BIN I DEPENDING ON THE CONDITIONS OF THE HB METHOD

KaPR / KuPR	Z_m > 18 dBZ at range bin i	Z_m < 18 dBZ at range bin i but some Z_m's are larger than 18dBZ above range bin i.	Z_m < 18 dBZ at range bin i and above
Z_m > 18 dBZ at range bin i	DFR	k/Z_e at KuPR	k/Z_e at KuPR
Z_m < 18 dBZ at range bin i, but some Z_m's are larger than 18 dBZ above range bin i	k/Z_e at KaPR	DFR	k/Z_e at KuPR
Z_m < 18 dBZ at range bin i and above	k/Z_e at KaPR	k/Z_e at KaPR	None

Figure Captions

Fig. 1 Schematic figure of footprints observed by DPR. Blue pixels are type (A), red pixels are type (B), and purple pixels are type (C).

Fig. 2 Schematic figure of a DPR measurement of precipitation assumed in the synthetic dataset.

Fig. 3 The definition of nodes A to D for profile with a bright band and for profile without bright bands. In the former case, node A is defined by referring air temperature. In the latter case, nodes B and C are not defined.

Fig. 4 k/Z_e at 13.8 GHz as a function of D_m at nodes A, B, C, and D (the nodes are defined in Table I).

Fig. 5 Framework of the HB-DFR algorithm.

Fig. 6 DFR as a function of D_m at nodes A, B, C, and D.

Fig. 7 Evaluation of precipitation rates estimated by the HB-DFR algorithm in the IDL. Colored lines indicate the average of estimates for each category of TOL. The solid black line indicates the average of estimates for all pixels. Gray shading shows a two-dimensional histogram of truths and estimates for all pixels, whereas the darker color is used for higher populations.

Fig. 8 Evaluation of some precipitation-related variables estimated by the HB-DFR algorithm in the IDL: (a) KuPR PIA, (b) KaPR PIA, (c) D_m at the lowest range bin, and (d) KuPR *k*-adjustment factor at the lowest range bin.

Fig. 9 The same as Fig. 7, but for the STD.

Fig. 10 Evaluation of some precipitation related variables estimated by the HB-DFR algorithm in the STD: (a) KuPR PIA, (b) KaPR PIA, (c) D_m at the lowest range bin, and (d) KuPR *k*-adjustment factor at the lowest range bin (estimates after the 99^{th} iteration and those after the 100^{th} iteration are shown, but are mostly overlapped).

Fig. 11 Contours of DSD-related variables on the (D_m, dB$\langle Z_f \rangle^{\delta}$) plane: (a) dB$N_w$ and precipitation rate, (b) dB$\langle Z_f \rangle^{u}$ and dB$\langle Z_f \rangle^{a}$, (c) KuPR and KaPR *k*-adjustment factors for stratiform precipitation, and (d) KuPR and KaPR *k*-adjustment factors for convective precipitation. The DSD type categorizations are shown by background colors.

Fig. 12 Evaluation of precipitation rates estimated by the HB-DFR algorithm for pixels only with type-1 and type-2 range bins: (a) in the IDL and (b) in the STD.

Fig. 13 Averaged vertical profiles in the STD: (a) to (c) are for profiles with a bright band, and (d) to (f) are for profiles without bright bands. KuPR Z_m (truths) and Z_e (truths and estimates) are shown in (a) and (d), KaPR Z_m (truths) and Z_e (truths and estimates) are shown in (b) and (e), and precipitation rates (truths and estimates) are shown in (c) and (f).

Fig. 14 The framework of single-frequency algorithms as special cases of the HB-DFR algorithm; (a) KuPR algorithm and (b) KaPR algorithm.

Fig. 15 The same as Fig. 7, but for the MDL.

Fig. 16 The same as Fig. 13, but for the MDL.

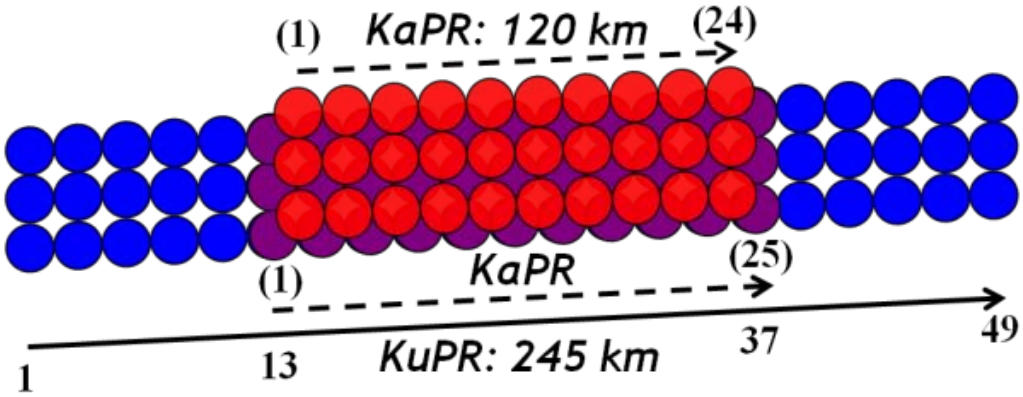

Fig. 1 Schematic figure of footprints observed by DPR. Blue pixels are type (A), red pixels are type (B), and purple pixels are type (C).

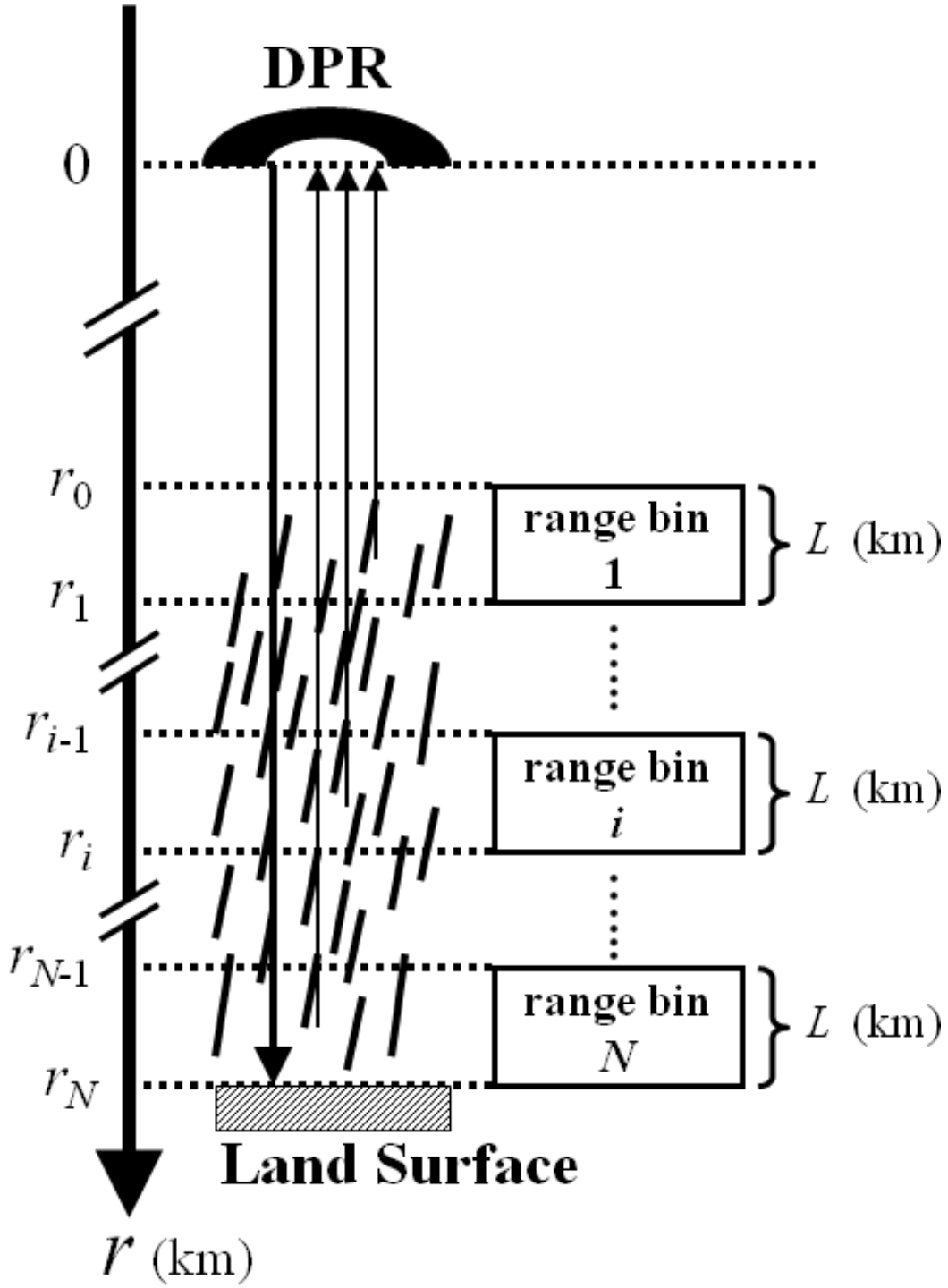

Fig. 2 Schematic figure of a DPR measurement of precipitation assumed in the synthetic dataset.

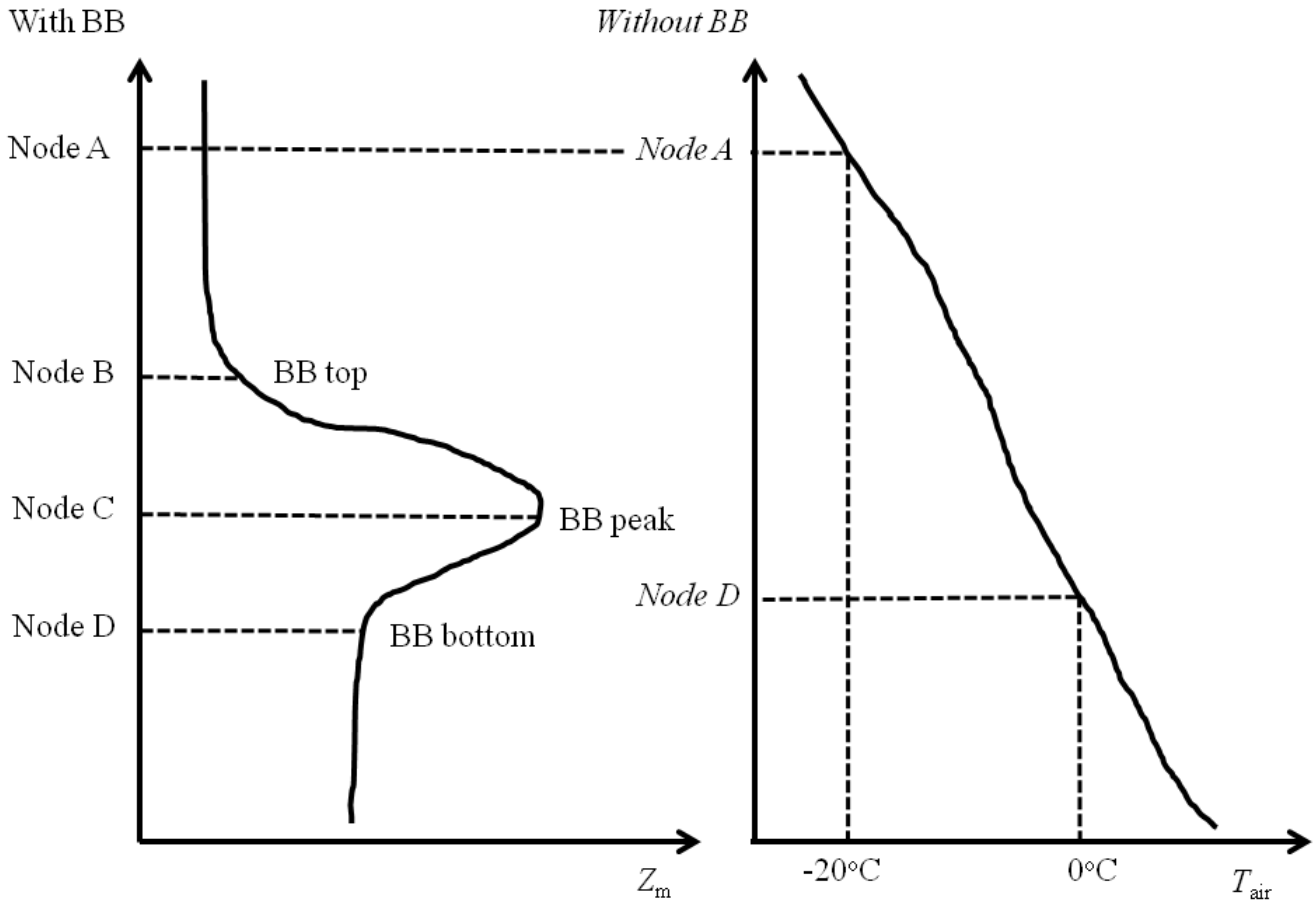

Fig. 3 The definition of nodes A to D for profile with a bright band and for profile without bright bands. In the former case, node A is defined by referring air temperature. In the latter case, nodes B and C are not defined.

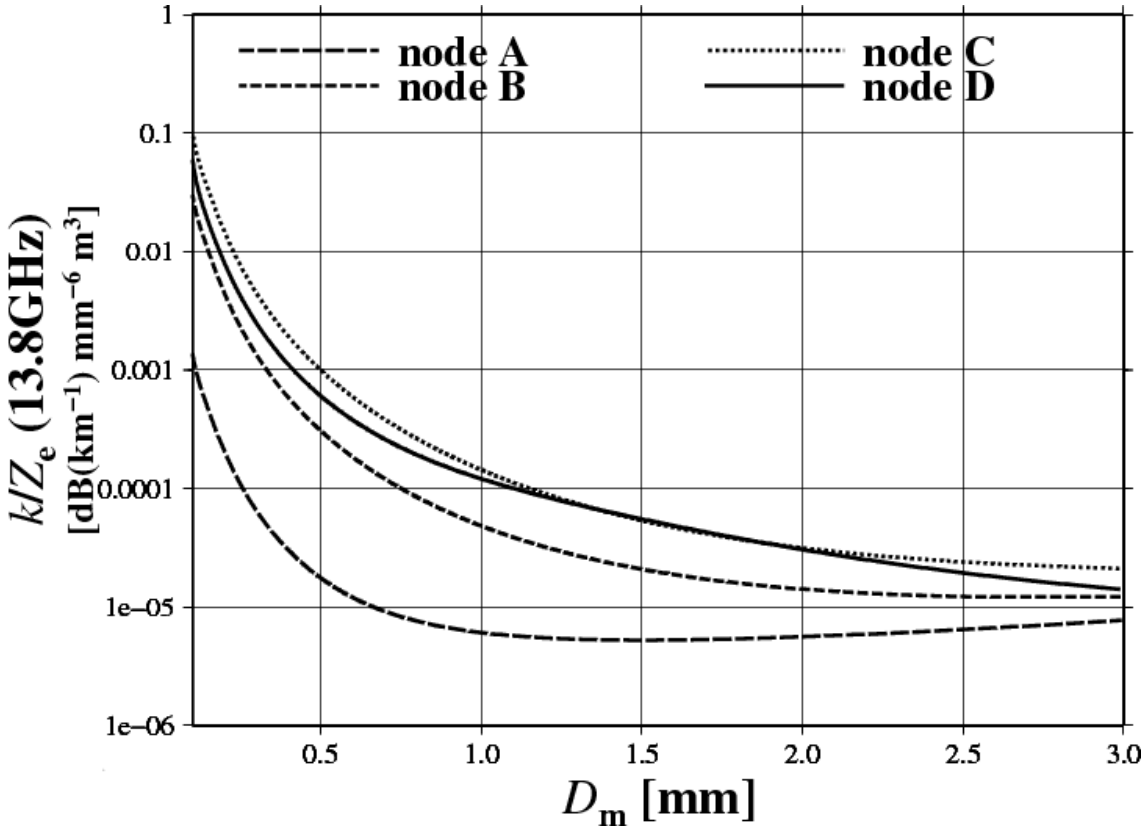

Fig. 4 k/Z_e at 13.8 GHz as a function of D_m at nodes A, B, C, and D (the nodes are defined in Table I).

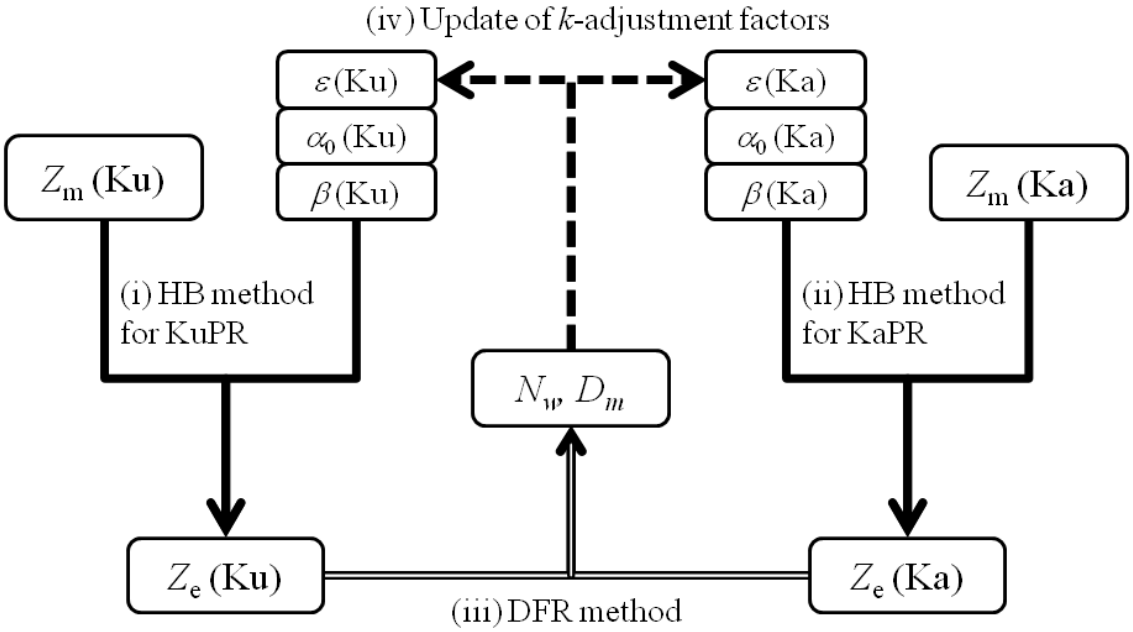

Fig. 5 Framework of the HB-DFR algorithm.

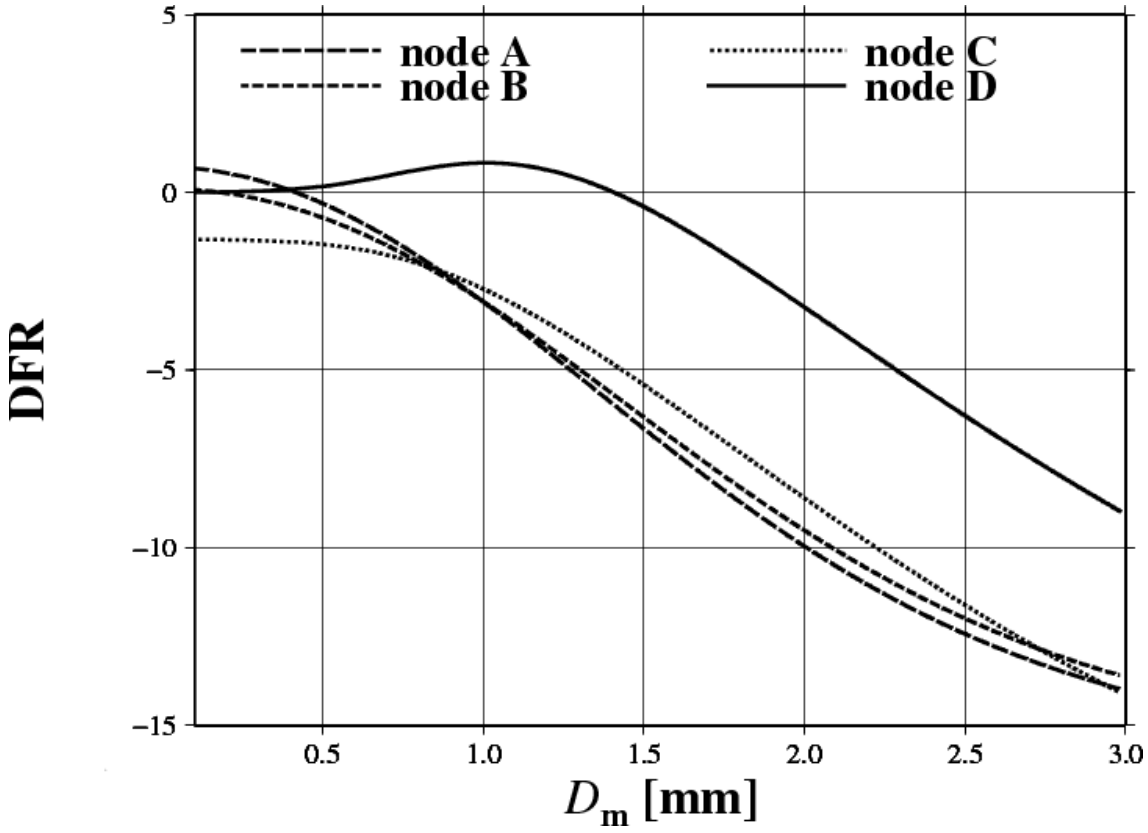

Fig. 6 DFR as a function of D_m at nodes A, B, C, and D.

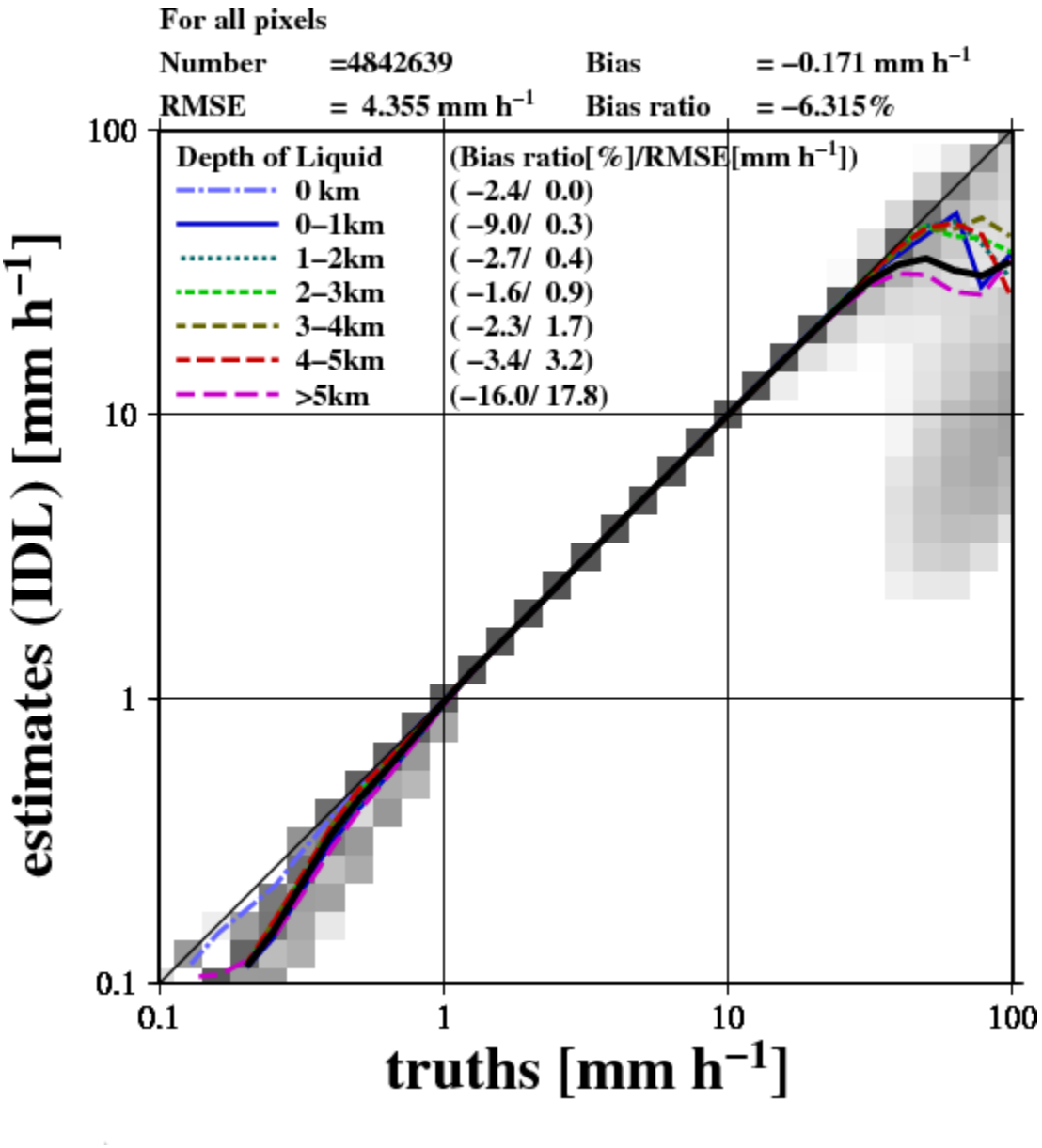

Fig. 7 Evaluation of precipitation rates estimated by the HB-DFR algorithm in the IDL. Colored lines indicate the average of estimates for each category of TOL. The solid black line indicates the average of estimates for all pixels. Gray shading shows a two-dimensional histogram of truths and estimates for all pixels, whereas the darker color is used for higher populations.

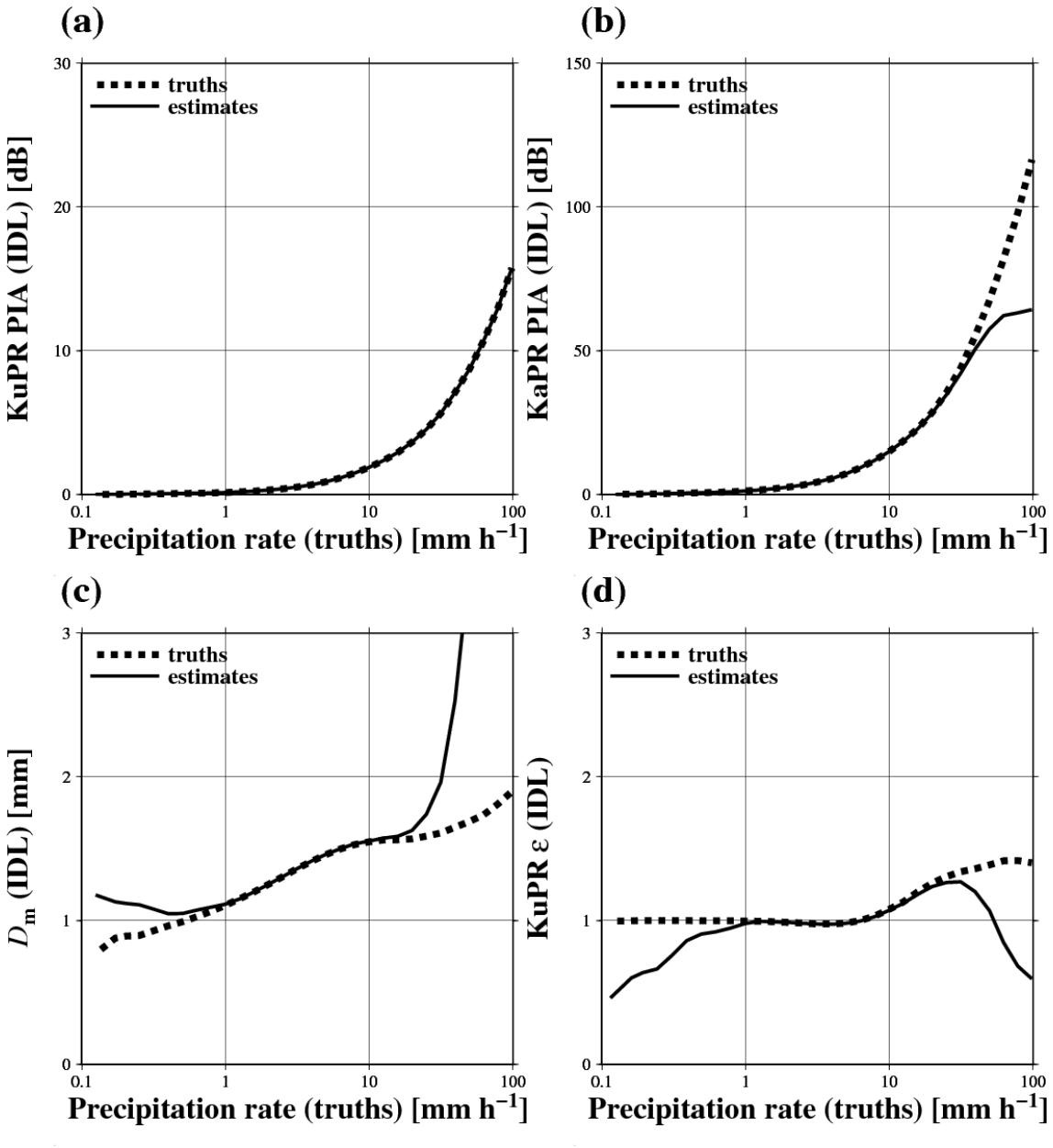

Fig. 8 Evaluation of some precipitation-related variables estimated by the HB-DFR algorithm in the IDL: (a) KuPR PIA, (b) KaPR PIA, (c) D_m at the lowest range bin, and (d) KuPR *k*-adjustment factor at the lowest range bin.

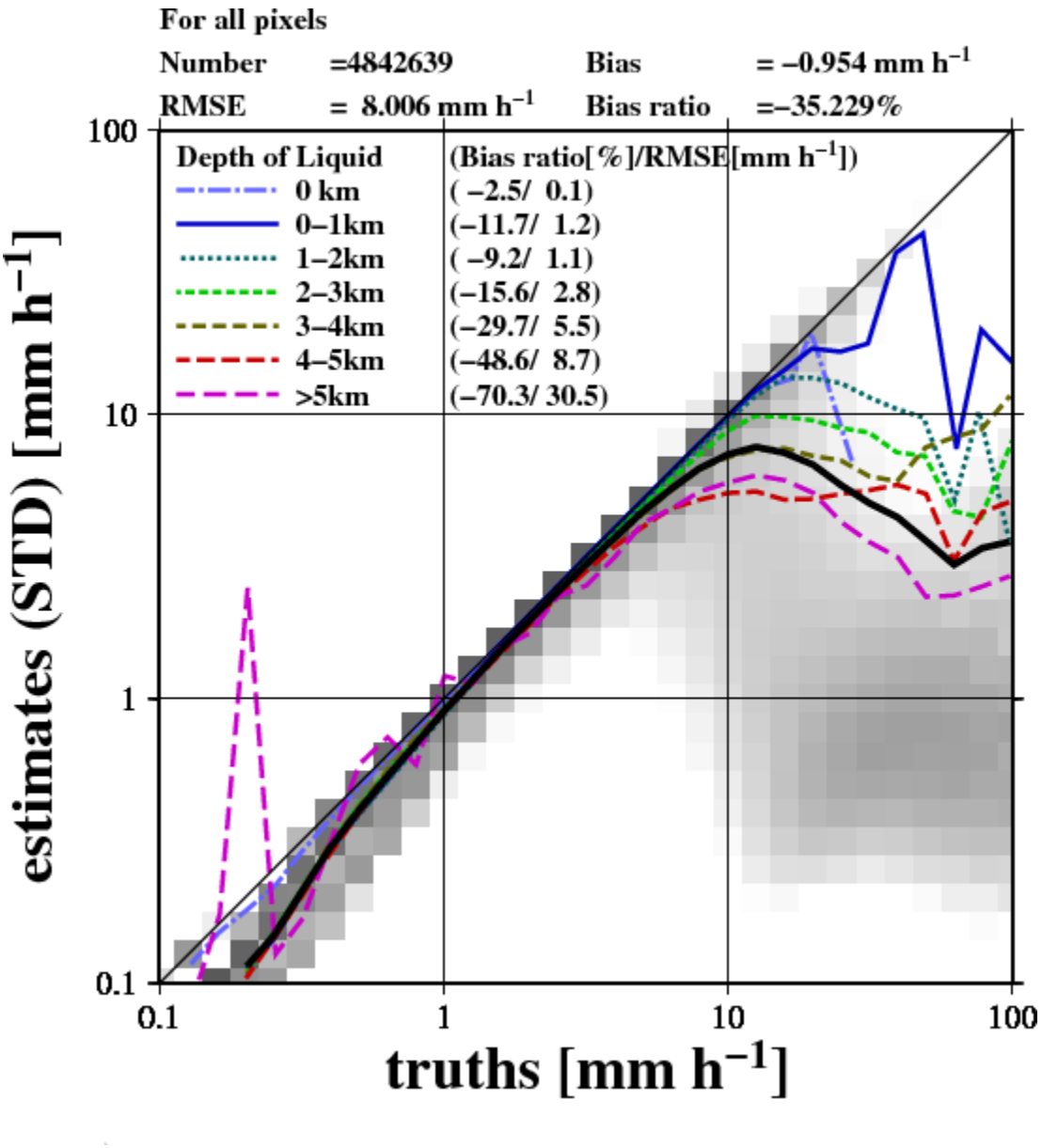

Fig. 9 The same as Fig. 7, but for the STD.

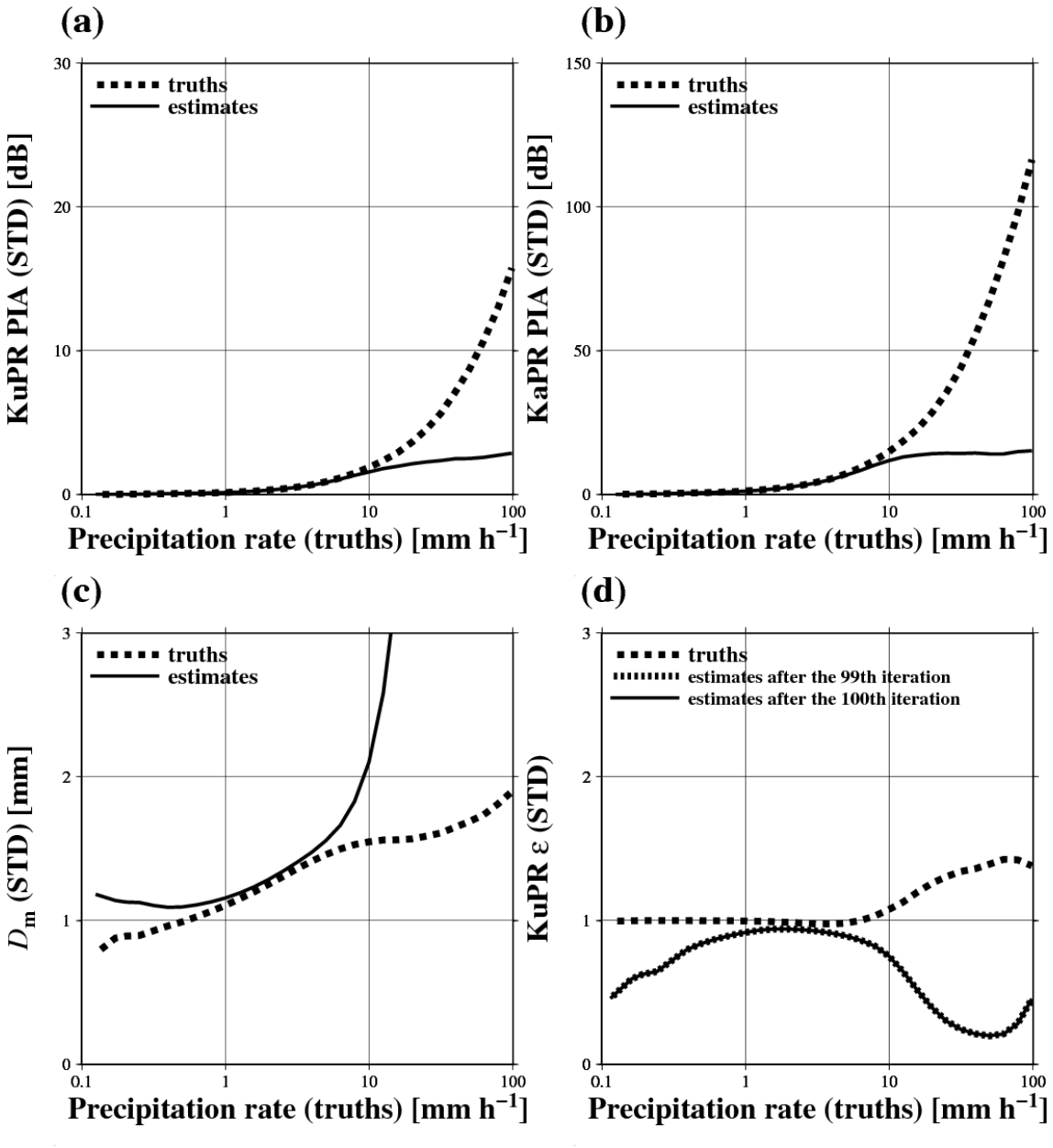

Fig. 10 Evaluation of some precipitation related variables estimated by the HB-DFR algorithm in the STD: (a) KuPR PIA, (b) KaPR PIA, (c) D_m at the lowest range bin, and (d) KuPR *k*-adjustment factor at the lowest range bin (estimates after the 99th iteration and those after the 100th iteration are shown, but are mostly overlapped).

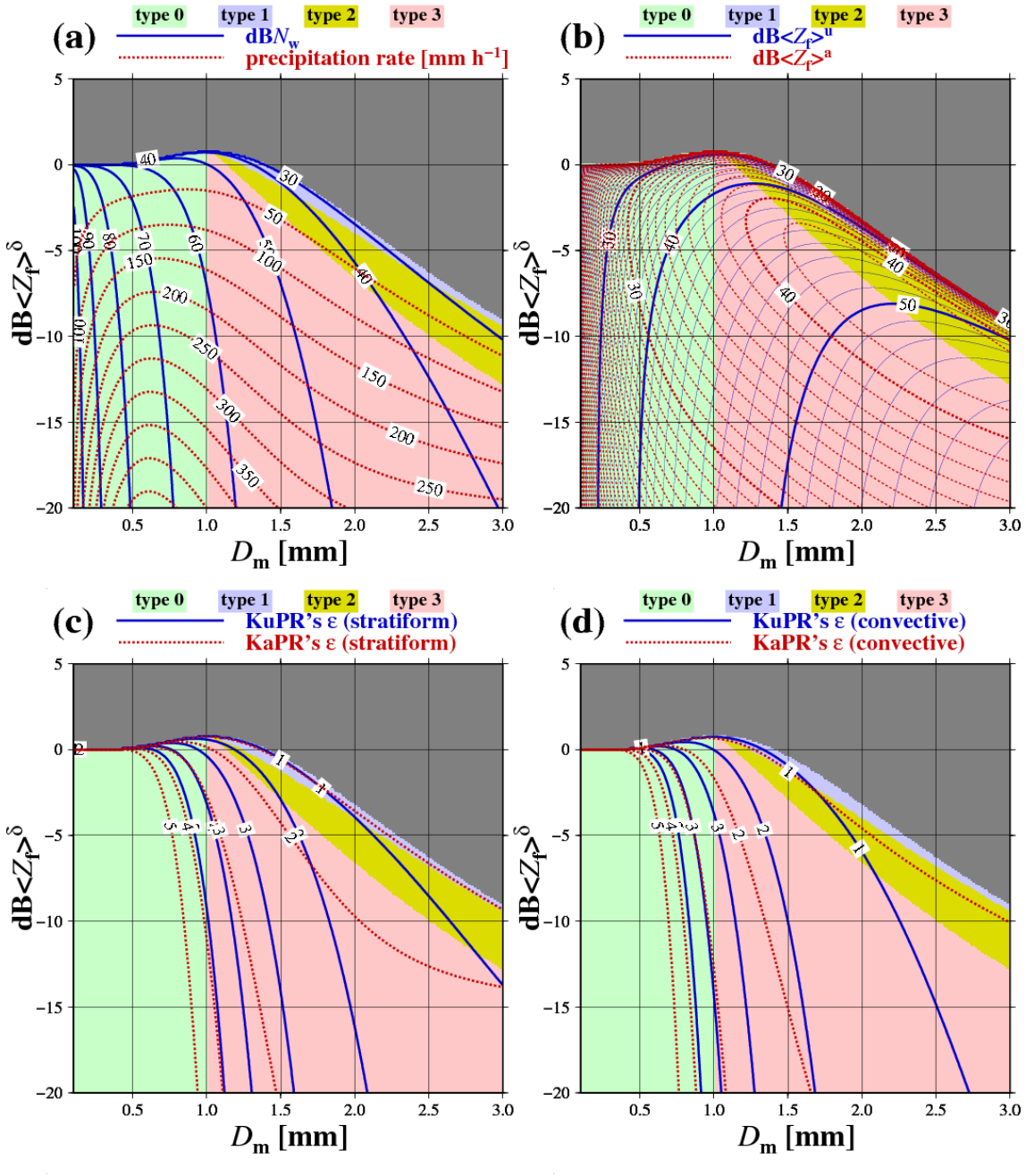

Fig. 11 Contours of DSD-related variables on the (D_m, dB<Z_f>$^\delta$) plane: (a) dBN_w and precipitation rate, (b) dB<Z_f>^{u} and dB<Z_f>^{a}, (c) KuPR and KaPR *k*-adjustment factors for stratiform precipitation, and (d) KuPR and KaPR *k*-adjustment factors for convective precipitation. The DSD type categorizations are shown by background colors.

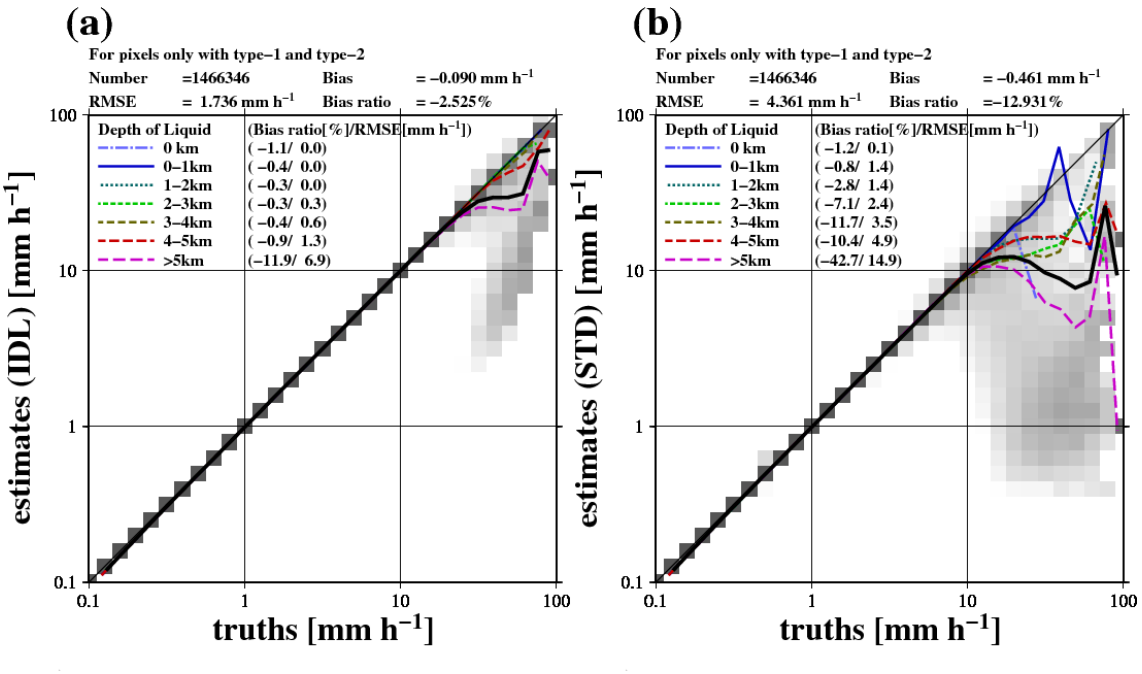

Fig. 12 Evaluation of precipitation rates estimated by the HB-DFR algorithm for pixels only with type-1 and type-2 range bins: (a) in the IDL and (b) in the STD.

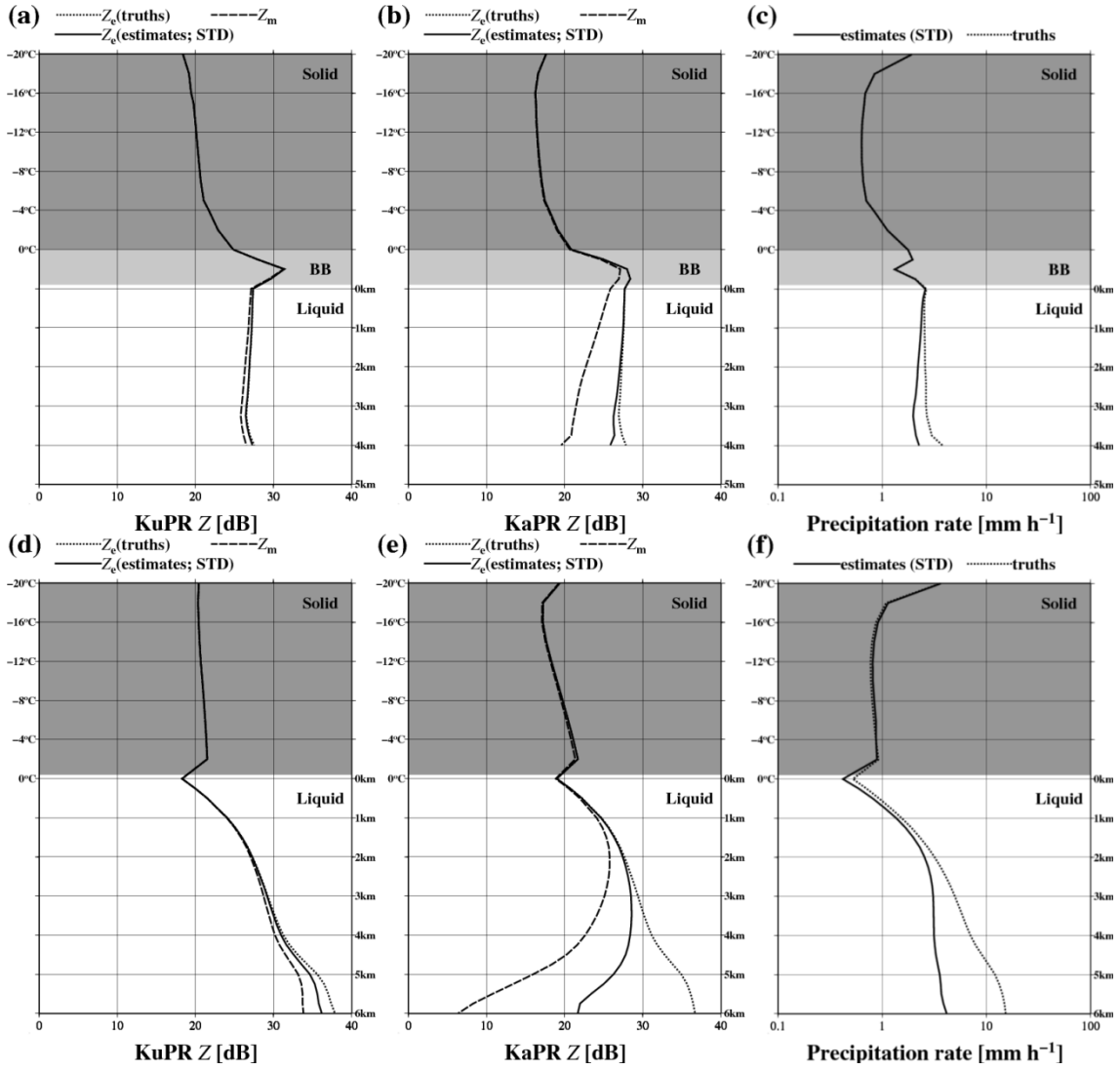

Fig. 13 Averaged vertical profiles in the STD: (a) to (c) are for profiles with a bright band, and (d) to (f) are for profiles without bright bands. KuPR Z_m (truths) and Z_e (truths and estimates) are shown in (a) and (d), KaPR Z_m (truths) and Z_e (truths and estimates) are shown in (b) and (e), and precipitation rates (truths and estimates) are shown in (c) and (f).

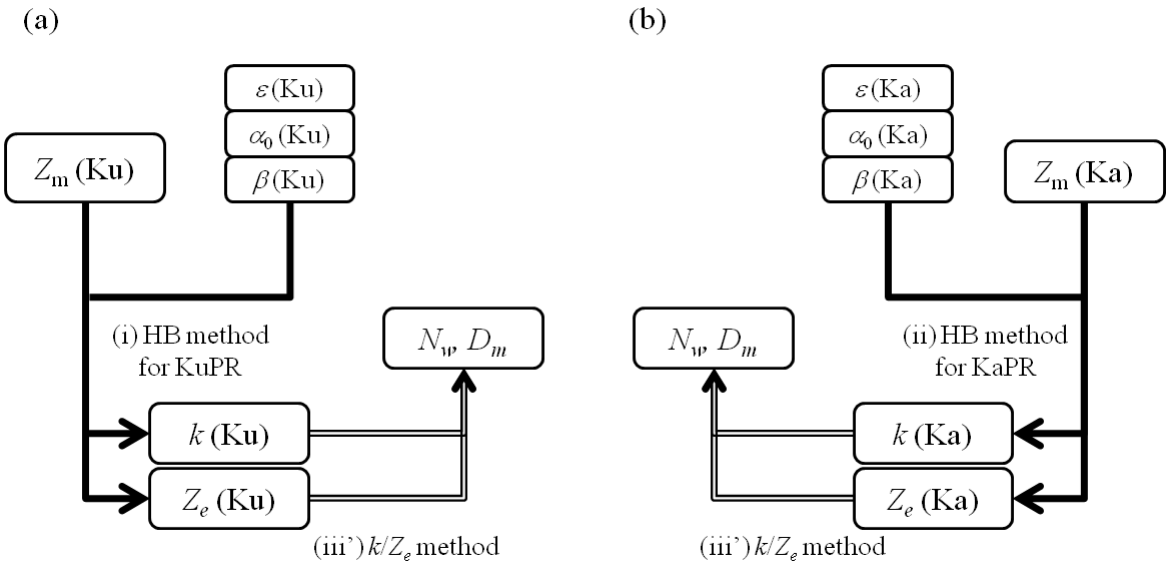

Fig. 14 The framework of single-frequency algorithms as special cases of the HB-DFR algorithm; (a) KuPR algorithm and (b) KaPR algorithm.

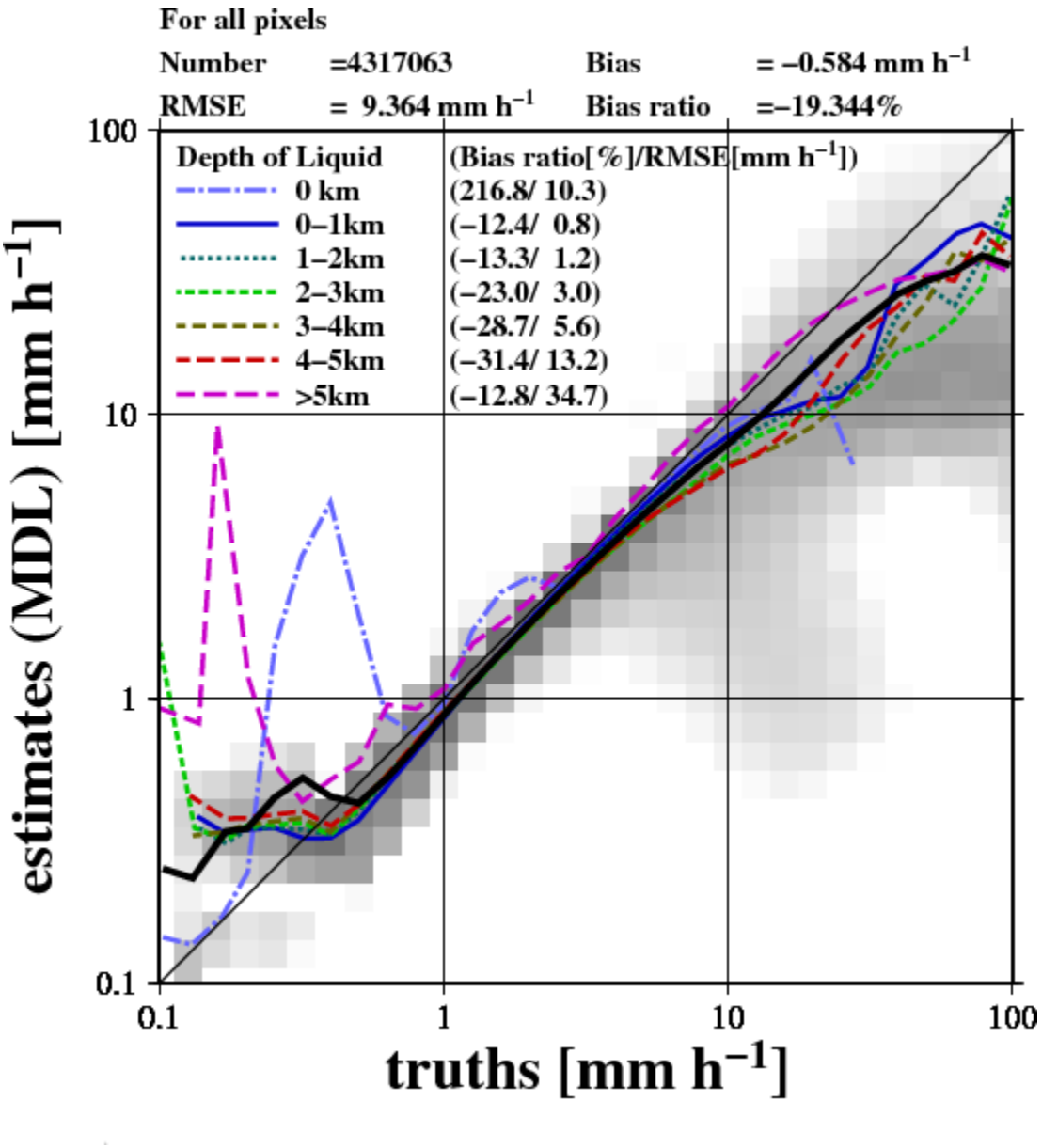

Fig. 15 The same as Fig. 7, but for the MDL.

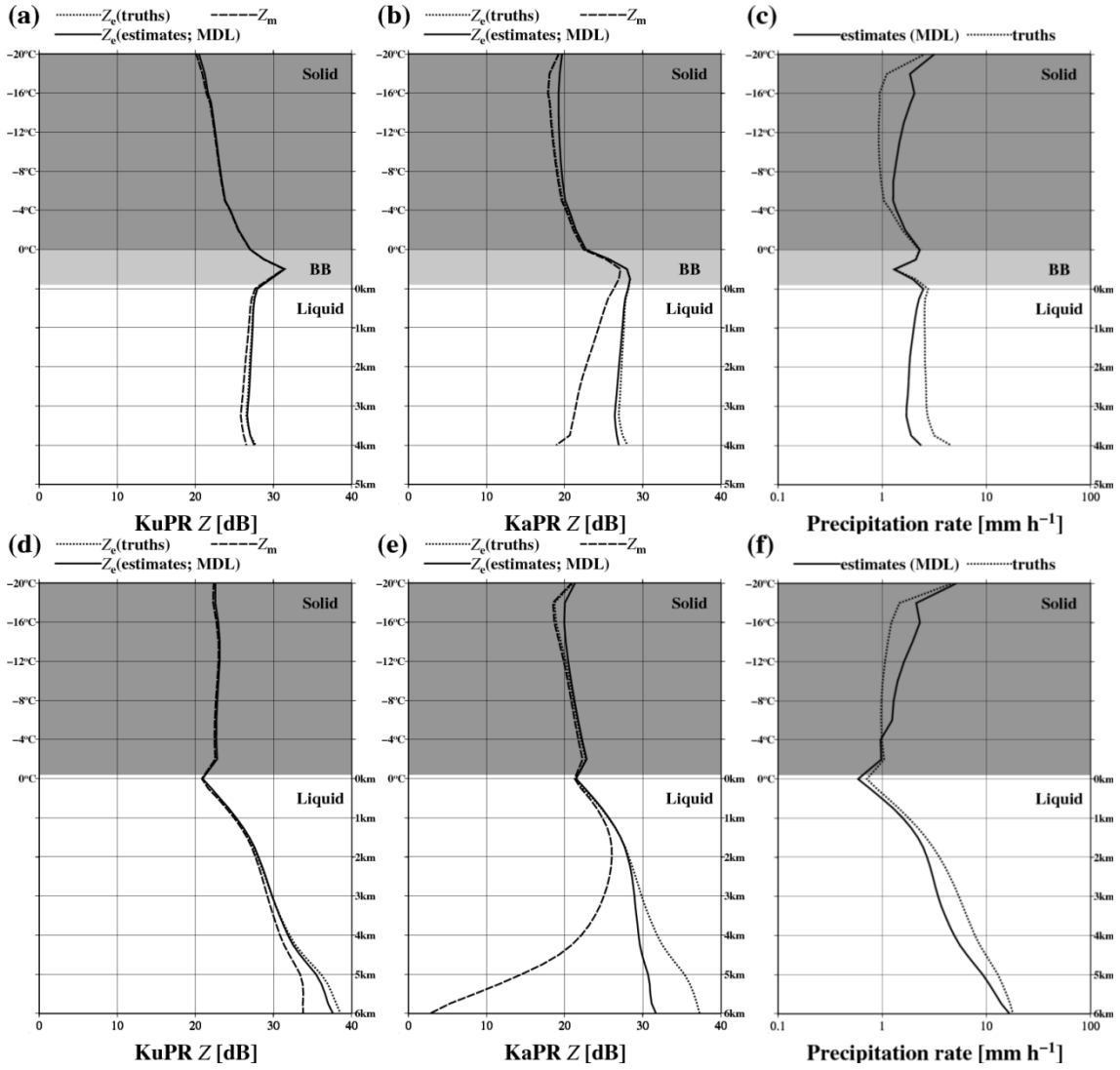

Fig. 16 The same as Fig. 13, but for the MDL.